
1 **Rapid oxidation of phenolic compounds by O₃ and**
2 **HO[•]: effects of air-water interface and mineral dust in**
3 **tropospheric chemical processes**

4
5
6 Yanru Huo^a, Mingxue Li^b, Xueyu Wang^c, Jianfei Sun^d, Yuxin Zhou^a,
7 Yuhui Ma^a, Maoxia He^{a,*}

8
9
10 ^a Environment Research Institute, Shandong University, Qingdao 266237,
11 P. R. China

12 ^b Department of Civil and Environmental Engineering, The Hong Kong
13 Polytechnic University, Hong Kong SAR, China

14 ^c College of Geography and Environmental Sciences, Zhejiang Normal
15 University, Jinhua 321004, China

16 ^d School of Environmental and Materials Engineering, Yantai University,
17 Yantai, 264005, PR China

18
19

*Corresponding author: Prof. Maoxia He

20 Tel: 86-532-58631972 (o)

21 Fax: 86-532-5863 1986

22 E-mail address: hemaox@sdu.edu.cn

23 Abstract

24 Environmental media affect the atmospheric oxidation processes of
25 phenolic compounds (PhCs) released from biomass burning in the
26 troposphere. To address the gaps in experimental research, phenol (Ph), 4-
27 hydroxybenzaldehyde (4-HBA), and vanillin (VL) are chosen as model
28 compounds to investigate their reaction mechanism and kinetics at the air-
29 water (A-W) interface, on TiO₂ mineral aerosols, in the gas phase, and in
30 bulk water using a combination of molecular dynamics simulation and
31 quantum chemical calculations. Of them, Ph was the most reactive one.
32 The occurrence percentages of Ph, 4-HBA, and VL staying at the A-W
33 interface are ~72%, ~68%, and ~73%, respectively. As the size of (TiO₂)_n
34 clusters increases, the adsorption capacity decreases until $n > 4$, and
35 beyond this, the capacity remains stable. A-W interface and TiO₂ clusters
36 facilitate Ph and VL reactions initiated by the O₃ and HO•, respectively.
37 However, oxidation reactions of 4-HBA are little affected by
38 environmental media because of its electron-withdrawing group. The O₃-
39 and HO•-initiated reaction rate constant (k) values follow the order of A-
40 $W_{Ph} > TiO_2_{VL} > A-W_{VL} > A-W_{4-HBA} > TiO_2_{4-HBA} > TiO_2_{Ph}$ and $TiO_2_{VL} >$
41 $A-W_{Ph} > A-W_{VL} > TiO_2_{4-HBA} > TiO_2_{Ph} > A-W_{4-HBA}$, respectively. Some
42 byproducts are more harmful than their parent compounds, so should be
43 given special attention. This work provides key evidence for the rapid
44 oxidation observed in the O₃/HO• + PhCs experiments at the A-W interface.

45 More importantly, differences in oxidation of PhCs by different
46 environmental media due to the impact of substituent groups were also
47 identified.

48 **Keywords:** Air-water interface; Titanium dioxide (TiO₂); Phenolic
49 Compounds; Adsorption mechanisms; Molecular dynamics (MD).

50 **1. Introduction**

51 Biomass burning, stemming from natural wildfires and human activity,
52 significantly contributes to atmospheric particulate matter (PM). Biomass
53 burning is a primary source of approximately 90% of the global primary
54 organic aerosols (POA) and releases a substantial quantity of organic
55 pollutants (Ito and Penner, 2005; Chen et al., 2017; Chen et al., 2023).
56 Biomass burning is to blame for about 62% of total annual emissions of
57 about 8.0 Tg of black carbon and 93% of total annual emission of about
58 33.9 Tg of organic carbon worldwide (Bond et al., 2004). Emissions from
59 biomass combustion are one of the primary sources of atmospheric and
60 particle pollutants that negatively affect human health, air quality, and
61 climate (Reid et al., 2005; Yao et al., 2016). One of the three main types of
62 biopolymers responsible for the formation of biomass is lignin (Sun et al.,
63 2011), also the polymeric organic molecule most abundant in plants (Lou
64 et al., 2010; Soongprasit et al., 2020). Pyrolysis of lignin releases phenolic
65 compounds (PhCs) into the air, including phenols, phenolic aldehydes, and
66 methoxyphenols. By mass, these PhCs make up between 21% and 45% of

67 the aerosol composition (Hawthorne et al., 1989; Diehl et al., 2013; Liao
68 et al., 2020; Soongprasit et al., 2020). Methoxyphenols are one of the
69 potential tracers that can be found in atmospheric wood smoke pollution,
70 with the emission rate ranging from 900 to 4200 mg kg⁻¹ fuel (Hawthorne
71 et al., 1989; Rogge et al., 1998; Simoneit, 2002; Chen et al., 2017).
72 Evidence shows that the oxidation processes of PhCs can result in the
73 formation of secondary organic aerosol (SOA) (Yee et al., 2013; Jiang et
74 al., 2023). Hence, it is imperative to explore the effects of PhCs when
75 exposed to atmospheric oxidants.

76 After being released into the atmosphere, PhCs will be oxidized by
77 ozone (O₃) and hydroxyl radicals (HO[•]). Both are significant contributors
78 to SOA (Arciva et al., 2022). The homogenous oxidation of PhCs has been
79 the emphasis of previous studies (Henry et al., 2008; Yee et al., 2013; Liu
80 et al., 2019; Arciva et al., 2022). Researchers investigated the kinetics and
81 reaction mechanisms of gas-phase interactions of PhCs with O₃ and HO[•] in
82 the past decade (Kroflič et al., 2018; Smith et al., 2016; Sun et al., 2021a;
83 Sun et al., 2021b; Liu et al., 2022). Furthermore, they investigated the
84 hydroxylation, ring opening, and oligomerization processes of PhCs in the
85 atmospheric liquid phase, with a focus on the potential environmental
86 toxicity and climatic effects of these events (Ma et al., 2021; Liu et al.,
87 2022; Arciva et al., 2022; Carena et al., 2023).

88 However, there is a dearth of specific data as well as explanations of

89 the mechanisms involved in the atmospheric oxidation of PhCs at the air-
90 water (A-W) interface. The atmosphere contains a high concentration of
91 aqueous aerosols and water microdroplets (Zhong et al., 2019; Guzman et
92 al., 2022). The oxidation of PhCs can rapidly occur at A-W interface (Rana
93 and Guzman, 2022b). The term "water surface catalysis" denotes the
94 phenomenon where chemical reactions happen at a faster rate at A-W
95 interface compared to the bulk phase (Lee et al., 2015a; Lee et al., 2015b;
96 Yan et al., 2016; Banerjee et al., 2017). In chemical engineering, titanium
97 dioxide (TiO₂) is an essential photoactive component found in atmospheric
98 mineral dust (Sakata et al., 2021; Wang et al., 2023). The interaction
99 between PhCs and TiO₂ is continuous (Grassian, 2009; Rubasinghege et
100 al., 2010; Shang et al., 2021), despite the relatively low prevalence of TiO₂
101 mineral particles (comprising 0.1% to 10% by mass). Therefore, it is
102 essential to investigate the disparity in the oxidation reaction mechanisms
103 and kinetics of PhCs at A-W interface and mineral dust particles.

104 **Increasing the number of constituents on the aromatic ring would affect**
105 **the reactivity and lead to complex compounds after reaction addition**
106 **and/or open ring pathways.** Phenol (Ph), 4-hydroxybenzaldehyde (4-HBA),
107 and vanillin (VL) are selected as model compounds to present
108 comprehensive mechanistic information at A-W interface, on TiO₂ clusters,
109 in the gas phase, and in bulk water, using a combination of molecular
110 dynamics simulation and quantum chemical calculations. Rate constants

111 were **calculated** throughout a wide temperature range in various EM.
112 Additionally, computational toxicology was employed to evaluate the
113 ecotoxicological impact of PhCs and their transformation products.

114 **2. Methods**

115 *2.1 Molecular dynamics simulation*

116 All of the molecular-dynamics simulations were carried out by utilizing
117 the GROMACS 2019 package, which included the AMBER force field.
118 Parametrization of the Ph, 4-HBA, and VL was accomplished by using the
119 GAFF force field in conjunction with RESP charge calculations performed
120 at the M06-2X/6-311++G(3df,2p)//M06-2X/6-31+G(d,p) level. The TIP3P
121 water model was utilized so that individual water molecules may be
122 represented (Jämbeck and Lyubartsev, 2014).

123 *2.1.1 Properties of Ph, 4-HBA, and VL at the A-W interface*

124 Considering the significance of the interfacial behavior of Ph, 4-HBA,
125 and VL at the A-W interface, the properties of these three substances were
126 initially examined by focusing on the A-W interface. **Fig. S1 (a)** depicts a
127 rectangular box that has dimensions of $4 \times 4 \times 9 \text{ nm}^3$ and has a Z-axis that
128 is perpendicular to the A-W contact. This box was used for all simulations.
129 **A water box that is too small may cause the central PhCs molecules to be**
130 **too close to the interface region, leading to inaccurate results. Conversely,**
131 **opting for a water box that is too large can lead to unnecessary waste of**
132 **computational resources.** To begin the process of constructing the initial

133 configurations, a water slab measuring $4 \times 4 \times 4 \text{ nm}^3$ was positioned at the
134 coordinates (2 nm, 2 nm, 4.5 nm) of the center of mass (COM). Because
135 the rest extension along the Z-axis of the box was sufficiently large (2.5
136 nm^3), it was possible to steer clear of the intersection of two A-W interface.
137 Prior to the formal simulation, six Ph molecules were randomly placed in
138 a vacuum above the water box for 150 nanoseconds of NVT molecular-
139 dynamics simulations. The results show that there are no significant π - π
140 interactions or formation of hydrogen bonds between the Ph molecules. To
141 simplify the model, this was followed by simulations of individual
142 molecules. Ph, 4-HBA, or VL were each placed in their own compartment
143 at the coordinates (2.0 nm, 2.0 nm, 7.75 nm) for each system in order to
144 simulate the behavior of these molecules in the A-W interface region of
145 **cloud/fog drops and aerosol liquid water (ALW)**. To begin, the three
146 different systems were optimized to use the least amount of energy possible.
147 After that, NVT molecular-dynamics simulations were carried out for a
148 total of 150 nanoseconds.

149 **2.1.2 Umbrella sampling simulations**

150 In **Fig. S1 (b)**, the molecule of Ph, 4-HBA, or VL was placed inside the
151 box (their COM is (2.00 nm, 2.00 nm, 6.00 nm)), which is located directly
152 2.00 nm away from the COM of the water slab. The distance between the
153 COM of Ph, 4-HBA, or VL and that of the water slab was used as the
154 definition for the reaction coordinate (**Fig. S1**). The weighted histogram

155 analysis approach, also known as WHAM, can be used to calculate the free
156 energy profiles of Ph, 4-HBA, or VL when they transition from the gas
157 phase into bulk water (Kumar et al., 1992; Hub et al., 2010) ; **details about**
158 **WHAM are in the Supporting Information Text S1.**

159 ***2.1.3 Radial distribution function***

160 Estimating the strength of hydrogen bonds (HB) between specific
161 atoms can be done with the help of a tool known as the radial distribution
162 function (RDF). **Text S2 has an explanation of the peculiarities of the RDF**
163 **and the coordination number.**

164 ***2.2 DFT calculations***

165 In this work, all **structural optimization and energy calculation** were
166 accomplished by utilizing the Gaussian16 program (Frisch et al., 2016). By
167 benchmarking at the CCSD(T)/cc-pVDZ, CBS-QB3, B3LYP/6-
168 311+G(d,p), MP2/6-311+G(d,p) and M06-2X/6-311+G(d,p) levels, Cao et
169 al. (Cao et al., 2021) found that M06-2X/6-311++G(3df,2p)//M06-2X/6-
170 31+G(d,p) is reliable for PhCs **at gas phase**. Therefore, all calculations for
171 gas-phase reactions are performed at this level. **Text S3** contains a
172 description of the additional calculated details. Multiwfn (Lu and Chen,
173 2012) was used to construct the electron density map. This program
174 integrates Visual Molecular Dynamics (version 1.9.3) (Humphrey et al.,
175 1996) in order to conduct an analysis of the electrostatic potential (ESP)
176 and the average local ionization energy (ALIE).

177 **2.3 IRI analysis**

178 Interaction Region Indicator (IRI) (Lu and Chen, 2021) was used to
179 determine the chemical bonds and weak interactions of Ph/4-HBA/VL
180 adsorbed to TiO₂ clusters (the details are in **Text S4**).

181 **2.4 Kinetic calculations**

182 **Text S5** contains an explanation of the kinetic calculation methods.

183 **3. Result and discussion**

184 **3.1 Enrichment of Ph, 4-HBA, and VL at the A-W interface**

185 **3.1.1 The uptake of gaseous PhCs at the A-W interface**

186 **Fig. S1** and **Fig. S2** illustrate the relative distributions of water, O₃, and
187 PhCs molecules (Ph, 4-HBA, and VL) in the A-W interface system along
188 the z-axis. HO[•] are primarily situated at the A-W interface contact, with the
189 potential to diffuse through the water slab interior (Roeselová et al., 2004).

190 **Fig. 1(a)** displays the variation in water density along the Z-coordinate
191 distance from 0 to 9 nm, categorizing three zones: A-W interface (2.25 to
192 2.79 nm and 6.21 to 6.75 nm), air (0 to 2.25 nm and 6.75 to 9 nm), and bulk
193 water (2.79 to 6.21 nm). This method accurately determines the interfacial
194 range (Zhang et al., 2019; Shi et al., 2020). According to location
195 definitions, O₃ percentage distribution was as follows: 26% at the A-W
196 interface; 72% in the air; and 2% in **bulk** water (**Fig. 1(b)**). **Fig. 1(c)** depicts
197 MD trajectories of Ph diffusion through the water slab from the air region
198 over a 150 ns period. Ph is distributed in the air (8%) and bulk water (20%),

199 with the majority at the A-W interface (72%) (**Fig. 1 (d)**). The majority of
200 4-HBA and VL molecules are located at the A-W interface, constituting 68%
201 and 73% of the total locations as presented in **Fig. S2**.

202 In **Fig. 2(a)**, we observe the three key processes involving PhCs (Ph,
203 4-HBA, or VL) diffusing into the water slab from the air region. (I) The
204 mutual attraction of gaseous Ph, 4-HBA, or VL; (II) The uptake of PhCs
205 (Ph, 4-HBA, or VL) at the A-W interface; (III) The hydration reaction of
206 PhCs (Ph, 4-HBA, or VL) in the bulk water. **Fig. 2(b)** displays the free
207 energy profile of the trajectories as Ph/4-HBA/VL transitions from the air
208 into the bulk water (see **Text 6** for calculations details). The $\Delta G_{\text{gas} \rightarrow \text{interface}}$
209 values are $-0.22 \text{ kcal mol}^{-1}$ for the Ph-A-W (Phenol-Air-Water) system,
210 $-0.45 \text{ kcal mol}^{-1}$ for the **A-W_{4-HBA}** (4-hydroxybenzaldehyde at Air-Water)
211 system, and -0.20 mol^{-1} for the **A-W_{VL}** (Vanillin-Air-Water) system. **This**
212 **finding is consistent with previous studies about Per-and poly-fluoroalkyl**
213 **substances (PFAS) at A-W interface (Yuan et al., 2023)**. These values
214 suggest that it is thermodynamically favorable for PhCs to approach the
215 interfacial water molecules. **Fig. S3** illustrates typical snapshots from the
216 trajectories of PhCs (Ph, 4-HBA, or VL). Initially, one molecule of Ph, 4-
217 HBA, or VL was placed in the center of the water box, with an equivalent
218 COM distance of 2 nm between the PhCs and the air phase. Subsequently,
219 the PhCs moved closer to the interface, leading to adsorption at the A-W
220 interface. **During the adsorption process, the H atom of the phenolic**

221 hydroxyl group binds to the oxygen atom of the H₂O molecules at the A-
222 W interface, forming H bonds and preventing its return to the bulk water.
223 This property allowed the phenolic hydroxyl groups on PhCs can
224 effectively adhere to the A-W interface, consistent with the experimental
225 observations using steady-state interfacial vibrational spectra (Kusaka et
226 al., 2021) and Fourier transform infrared (FTIR) imaging micro-
227 spectroscopy (Guzman et al., 2022). Based on these findings, compared to
228 the number of PhCs molecules distributed in the gas phase and in bulk
229 water, the location where air and water meet exhibits an increased the
230 number of PhCs molecules.

231 *3.1.2 Interface properties of PhCs*

232 Introducing more hydrophilic functional groups increases the
233 characteristic angle α and β of PhCs at the interface, allowing for more
234 secure adsorption at the water-air interface. The interaction between H_{PhCs}
235 and O_{H₂O} is the primary factor influencing the stability of PhCs at the
236 interface. The coordination number (N) of H_{Ph-OH-O_{H₂O}}, H_{4-HBA-OH-O_{H₂O}},
237 and H_{VL-OH-O_{H₂O}} are 2.68, 2.51, and 2.09 respectively. The number of
238 functional groups attached to the benzene ring affects the N value; more
239 functional groups lead to a lower N value. The reason is that aldehyde and
240 methoxy are strong electron-withdrawing groups, which will reduce the
241 conjugation effect between the benzene ring and the hydroxyl group,
242 making the hydrogen atom on the hydroxyl group partially positively

243 charged, thus weakening the hydrogen bonding ability with water
244 molecules. See **Text S7** for interface properties of PhCs.

245 **3.2 Adsorption of Ph, 4-HBA, and VL by TiO₂ Clusters**

246 The placement of PhCs on TiO₂ clusters significantly impacts
247 adsorption energies (Bai et al., 2020). The adsorption capacity of pollutants
248 on cluster surfaces is a key factor influencing degradation efficiency (Qu
249 and Kroes, 2006). The primary mechanism of C atoms adsorption to
250 (TiO₂)_n (n = 1–4) clusters occurs at a range of 2.57 to 2.61 Å and involves
251 interaction between the H_{-OH} atom and the O_{TiO₂} atom, as seen in **Fig. 3(a)**.
252 Hydrogen bonds can be formed between the H_{-OH} atom and the O_{TiO₂} atom
253 (1.80–2.61 Å), improving the adsorption capacity. In contrast, Ph
254 adsorption to (TiO₂)_n (n = 5–6) clusters, ranging from 2.08 to 2.09 Å, is
255 primarily due to interaction between Ti atom and O_{-OH} atom. **For a detailed**
256 **description see Text S8.**

257 Adsorption energy a metric of adsorption capacity, is illustrated in **Fig.**
258 **3(b)–(d)** for Ph, 4-HBA, and VL on (TiO₂)_n (n = 1–6). TiO₂ exhibits the
259 highest adsorption capacity for Ph. ($\Delta G_{\text{ad}} = -72.35 \text{ kcal mol}^{-1}$) (**Fig. 3(b)**).
260 The adsorption energy values of TiO₂ and (TiO₂)₃ for 4-HBA and VL are
261 -45.32 (**Fig. 3(c)**) and $-102.46 \text{ kcal mol}^{-1}$ (**Fig. 3(d)**), respectively.
262 **Physisorption energy range from -1.20 to $9.56 \text{ kcal mol}^{-1}$ (Nollet et al.,**
263 **2003), thus this adsorption process in this study is spontaneous chemical**
264 **adsorption.** However, the capacity of TiO₂ to adsorb VL is significantly

265 higher than that to adsorb Ph and 4-HBA. **Fig. 3(b)–(d)** show that the
266 adsorption capacity falls as the size of TiO_2 clusters increases when $n \leq 4$.
267 In contrast, the adsorption capacity remains constant when $n > 4$. IRI
268 measurements of Ph on the $(\text{TiO}_2)_n$ surface (**Fig. 3(e)**) reveal Ph- TiO_2
269 hydrogen bonds ($\text{H}_{\text{Ph}}-\text{O}_{\text{TiO}_2}$ bonds) and their electrostatic and dispersion
270 effects. Benzene C atom of Ph exhibits sp^2 hybridization, meaning it forms
271 one σ -bond and one π -bond. The sp^2 hybridization of benzene for Ph
272 explains its limited interaction with TiO_2 clusters and accounts for the
273 substantial adsorption energy. Similar interactions occur with 4-HBA and
274 VL (**Fig. S7**). Hydrogen bonds form between the H_{CHO} atom of 4-HBA or
275 VL and the O_{TiO_2} atom, despite the presence of the H_{Ph} atom.

276 **3.3 Continuous oxidation mechanisms**

277 **3.3.1 O_3 - and HO^\bullet -initiated reactions**

278 PhCs, once released into the atmosphere, undergo several processes,
279 including adsorption on mineral aerosol surfaces, accumulation at the A-W
280 interface, dispersion in bulk water within liquid droplets, and oxidation
281 reactions initiated by atmospheric oxidants (Lin et al., 2017). This section
282 delves into the detailed mechanisms and characteristics of these reactions.
283 At the M06-2X/6-311++G(3df,2p)//M06-2X/6-31+G(d,p) level, the
284 structures with the minimum free energy for the Ph/4-HBA/VL has been
285 determined (**Fig. S10**). In the case of VL, a significant reduction in
286 molecular energy is observed due to the formation of a powerful

287 intramolecular hydrogen bond with a length of 2.09 Å between the H and
288 O atoms near the methyl group. Moreover, the lone pair electrons of
289 oxygen atoms can form additionally p- π conjugations with the π electrons
290 of the phenyl ring, further reducing the overall energy of VL in gas phase.
291 The statistical charts of calculated $\Delta_r G$ and ΔG^\ddagger values for O₃- and HO•-
292 initiated reactions are displayed in **Fig. 4** and **S8** and detailed data are
293 available in **Tables 1–4**.

294 O₃ is a major oxidant in the atmosphere, with high concentrations in
295 the troposphere ranging between 9.85×10^{11} molecules cm⁻³ (Tomas et al.,
296 2003; Pillar-Little et al., 2014). Investigating the fate of PhCs in the
297 presence of O₃ is essential (Pillar-Little et al., 2014; Rana and Guzman,
298 2020). The ozonolysis of PhCs involves the synthesis of primary ozonide,
299 the formation of active Criegee intermediate (CI), and the disintegration of
300 CI (Rynjah et al., 2024). The O₃-initiated reactions of Ph/4-HBA/VL
301 involve radical adduct formation (RAF) channels on their benzene ring
302 (R_{O₃-RAF}1–6), highlighted in red in **Fig. S10**. **Fig. 4(a)–(d)** depict that the
303 ozonolysis pathways R_{O₃-RAF} are exergonic, indicating their spontaneity.
304 The average ΔG^\ddagger values for the ozonolysis of Ph/4-HBA/VL are ranked as
305 Ph > VL > 4-HBA. The following is a list of the average values for the
306 ozonolysis of Ph/4-HBA/VL, as illustrated in **Fig. 4(e)–5(h)**, Ph is superior
307 to VL and 4-HBA, with the exception on TiO₂ clusters. **Fig. 4(e)** illustrates
308 that the average value of ΔG^\ddagger for O₃ + Ph reactions at the A-W interface is

309 15.38 kcal mol⁻¹, the lowest value out of the three PhCs. The average ΔG^\ddagger
310 values for the ozonolysis of Ph/4-HBA/VL are as follows: VL (13.95 kcal
311 mol⁻¹) < Ph (24.70 kcal mol⁻¹) < 4-HBA (25.16 kcal mol⁻¹) on TiO₂
312 clusters (**Fig. 4(f)**). The average ΔG^\ddagger values for O₃ + VL reactions in gas
313 phase are the highest among the four different EM (23.28 kcal mol⁻¹)
314 shown in **Fig. 4(g)**). Comparing the phenolic oxidation in each of these
315 four EM (bulk water, interface, TiO₂ clusters, and gas phase) reveals that
316 A-W interface are more conducive to the ozonolysis of Ph, whereas TiO₂
317 clusters are more conducive to the ozonolysis of VL. The effect of
318 solvation on ΔG^\ddagger is predominantly caused by the hydration of the phenolic
319 OH group, as this is the part of the molecule being solvated. However, the
320 presence of water molecules in the region around the phenyl group has
321 been shown to have a considerable influence on the ΔG^\ddagger values.

322 HO[•], known as "atmospheric detergents", is another significant
323 atmospheric oxidant (Atkinson, 1986; Zhang et al., 2020). **The worldwide**
324 **mean tropospheric concentration of HO[•] is roughly 11.3×10^5 molecules**
325 **cm⁻³ (Lelieveld et al., 2016).** For this reason, elucidating the reaction
326 mechanism underlying HO[•] + PhCs reactions in the troposphere is of the
327 utmost importance. HO[•]-initiated reaction pathways of Ph/4-HBA/VL
328 include RAF, hydrogen atom abstraction (HAA) channels from the
329 benzene ring (R_{HAA}ben1–6) and the substituent group (R_{HAA}sub7–9).
330 Previous research (Gao et al., 2019) has shown that the process of single

331 electron transfer (SET) does not significantly contribute to the HO[•]-
332 initiated reactions examined. Once the hydroxyl adducts or H₂O are formed,
333 significant heats (4.21–30.28 kcal mol⁻¹) are released (**Fig. 4(i)–(l), S8**
334 **(a)–(d) and (i)–(l)**); the detail data in **Table S3**), indicating high
335 thermodynamic feasibility. The average ΔG^\ddagger values for HO[•]-initiated
336 reactions (**Fig. 4(m)–(p), S8 (e)–(h) and (m)–(p)**) are lower than those for
337 O₃-initiated reactions. Routs R_{HAA}ben make a minimal contribution to HO[•]-
338 initiated reactions. At the A-W interface, VL (3.52 kcal mol⁻¹) < Ph (4.52
339 kcal mol⁻¹) < 4-HBA (9.50 kcal mol⁻¹), and the ΔG^\ddagger value of Ph is the
340 lowest (-0.97 kcal mol⁻¹), the case for pathways R_{RAF-HO[•]} (**Fig.4(m)**).
341 Among the three aromatic compounds, the R_{RAF-HO[•]} routes of VL on TiO₂
342 clusters are the most favorable (**Fig. 4(n)**). When compared to HO[•]-
343 initiated reactions of aromatic compounds in the gas phase (**Fig. S9(e)**) or
344 bulk water (**Fig. S9(f)**), the process of Ph + HO[•] reactions at the A-W
345 interface is accelerated, whereas the process of VL + HO[•] reactions is
346 accelerated by TiO₂ clusters. These findings are in agreement with the
347 ozonolysis findings. The same guidelines can be used to routes R_{HAA}sub
348 (**Fig. 4(o), (p), S8 (g) and (h)**) and R_{HAA}ben (**Fig. S8(m)–(p)**). The
349 following is a ranking of the average ΔG^\ddagger values for routes R_{RAF-HO[•]} in the
350 gas phase or bulk water: Ph < 4-HBA < VL. As a result of having the lowest
351 ΔG^\ddagger values among all HO[•]-initiated reaction mechanisms, routes R_{RAF} are

352 the most advantageous of all the possible reaction mechanisms. In light of
353 this, each and every route R_{RAF-HO^\bullet} and R_{HAASub} will be dissected in detail.

354 **Fig. 5** shows the $\Delta_r G$ and ΔG^\ddagger values of O_3 - and HO^\bullet -initiated reactions
355 at various reaction locations. These reactions are almost entirely
356 exothermic, with a close correlation between $\Delta_r G$ values and ΔG^\ddagger values.
357 The ΔG^\ddagger values for the Phe + O_3 reactions shown in **Fig. 5(a)** are the lowest
358 among the three compounds, ranging from -0.97 to 7.86 kcal mol⁻¹.
359 Exergonic and spontaneous addition reactions took place at the C1–C2 and
360 C3–C4 locations of Ph and VL, respectively. Because of their low ΔG^\ddagger
361 values, the C1–C2 and C2–C3 sites of O_3 -initiated reactions for 4-HBA are
362 advantageous. Their values are 21.76 and 22.03 kcal mol⁻¹, respectively.
363 The C1–C2 location of 4-HBA is activated to a greater extent at the A-W
364 interface in comparison to the gas phase and bulk water. However, the ΔG^\ddagger
365 values of O_3 + Ph reactions on TiO_2 clusters are significantly greater than
366 those of the A-W interface (12.86 – 18.10 kcal mol⁻¹) than 24.30 – 25.34
367 kcal mol⁻¹. The VL + O_3 reactions on TiO_2 clusters are favorable at the
368 C2–C3 and C4–C5 locations (the ΔG^\ddagger values are 11.42 and 11.14 kcal mol
369 ⁻¹, respectively, **Fig. 5(b)**). This can be explained by the fact that the
370 electron cloud has a greater propensity to congregate in the places C2–C3
371 and C4–C5, respectively. In addition, the p orbitals of the methoxy and
372 hydroxy groups are conjugated to the benzene ring, which offers a
373 powerful electron-donating conjugation effect (Aracri et al., 2013).

374 Because of this, the oxidation of aromatic molecules is thermodynamically
375 more favorable than the oxidation of the aldehyde group. **This is consistent**
376 **with previous studies that electron density influences the oxidative activity**
377 **of PhCs (Rana and Guzman, 2022a).** Clearly, the ΔG^\ddagger values of HO \cdot -
378 initiated reactions ($-0.97\sim 13.46$ kcal mol $^{-1}$) in **Fig. 5(c)–(f)** are lower than
379 those of O $_3$ -initiated processes ($11.14\sim 27.83$ kcal mol $^{-1}$) at different points
380 in A-W interface and TiO $_2$ clusters. This can be seen by comparing the
381 values to each other. At the A-W interface, the most advantageous position
382 for the phenol hydroxyl group to be in for Ph/4-HBA/VL + HO \cdot reactions
383 are the ortho position (**Fig. 5(c)**). OESI-MS, which stands for online
384 electrospray ionization mass spectrometry, was also able to identify the
385 hydroxylation product known as 3,4-dihydroxybenzaldehyde (Rana and
386 Guzman, 2020). In **Fig. 5(d)**, the ortho- and meta-sites of phenol hydroxyl
387 are, respectively, the most favorable positions for Ph/4-HBA + HO \cdot
388 reactions on the TiO $_2$ clusters. On the other hand, all of the VL sites on the
389 TiO $_2$ clusters are advantageous. At the A-W interface and on the TiO $_2$
390 clusters, the abstraction of hydrogen atoms follows the order of H-CHO atom >
391 H-OCH $_3$ atom > H-OH atom in **Fig. 5(e) and (f)**. This can also be explained
392 by the ALIE values of these atoms listed in the same order of H-CHO atom
393 ($11.67\sim 11.74$ eV) > H-OCH $_3$ atom (14.06 eV) > H-OH atom (15.46 eV), as
394 shown in **Fig. S8**.

395 **3.3.2 Generation and degradation of key products**

396 For the purpose of this discussion, the primary atmospheric destiny of
397 the selected aromatic compounds was taken into consideration to be their
398 bimolecular reactions with O₂/O₃. **Fig. 6** and **S10** illustrate the subsequent
399 reaction mechanisms of IMs, respectively. IM₁₋₂ was produced using the
400 pathway that offered the best conditions for the HO[•]-initiated reaction of
401 Ph. As can be seen in **Fig. 6(a)**, the addition of O₂ to the C3 sites of the
402 C₆H₅O radicals results in the formation of C₆H₅O-OO radicals with no
403 barriers in either the gas phase or the bulk water. This is a desirable
404 outcome. **For the transformation of the C₆H₅O₂-OO radicals that were
405 created, the ring closure reaction to form C₆H₅O₂-OO-d is attractive option.**
406 However, it must overcome an energy barrier of 18.83 kcal mol⁻¹ in the
407 gas phase or 13.67 kcal mol⁻¹ in bulk water. The C₆H₅O₂-OO-d₁ radical,
408 which was produced by the C₆H₅O₂-OO-d reaction, interacts once more
409 with O₂. **In the atmosphere, these Criegee intermediates also may undergo
410 bimolecular reactions with NO_x (Sun et al., 2020).** Malealdehyde (P1) is
411 what should mostly result from the reaction of the C₆H₅O₂-OO-d₁ radical
412 with NO. However, during this process, it still needs to overcome an energy
413 barrier of 49.5 (in the gas phase) or 50.83 kcal mol⁻¹ (in the bulk water) to
414 generate C₆H₅O₂-OO-d₃ radical; as a result, the further transformation of
415 the formed C₆H₅O₂-OO-d₂ should continue very slowly. Pyrocatechol (P2)
416 is the primary product generated in the gas phase and bulk water when the
417 H atom of the C₆H₅O₂-OO radical is displaced. **P2 generates o-**

418 semiquinone radicals via pathways R_{HAA} by HO^\bullet or O_3 , which in turn
419 generate oligomers (Guzman et al., 2022). This results in the formation of
420 brown organic carbon in atmospheric aerosols. At the A-W interface, a
421 sequence of hydroxylation products, including pyrocatechol (P2), benzene-
422 1,2,3-triol (P3), and benzene-1,2,3,4,5-pentaol (P4), are generated through
423 hydroxylation processes rather than by a single SET ($\Delta G^\ddagger = 111.79$ kcal
424 mol⁻¹). It is difficult for P4 to form benzene-1,2,3,4,5,6-hexaol because
425 hydrogen transfer reactions are difficult to occur ($\Delta G^\ddagger = 34.32$ kcal mol⁻¹).
426 These hydroxylation products have been detected by experimental means
427 (Pillar-Little et al., 2014; Pillar-Little and Guzman, 2017; Rana and
428 Guzman, 2020). The HO^\bullet abstracts a hydrogen atom from the hydroxyl
429 group of catechol, forming $C_6H_5O_2$ radical and a water molecule. Due to
430 the widespread presence of NO_2 in the environment, it adds to the $C_6H_5O_2$
431 radical at the ortho position of the extracted hydrogen atom through an
432 addition reaction. Subsequently, a hydrogen transfer reaction occurs,
433 resulting in the formation of 4-nitrobenzene-1,2-diol (P_{2-a}). This
434 computational result validates the previous experimental hypothesis by
435 Finewax et al (Finewax et al., 2018). The P_{2-a} subsequently transform into
436 benzoquinone, maleic acid, fumaric acid, acetic anhydride, acetic acid, and
437 formic acid, or are directly mineralized into carbon dioxide and water
438 (Chen et al., 2015). In order to gain a more comprehensive understanding
439 of the reaction mechanism at the A-W interface, the major product (the

440 C₇H₅O₂ radical) for pathways R_{HAA} of 4-HBA was also taken into
441 consideration. According to **Fig. S11 (a)**, the addition of HO• to the C7
442 sites of the C₇H₅O₂ radical can occur without any obstructions. The
443 overpowering of the 18 kcal mol⁻¹ barrier resulted in the formation of the
444 hydroxylation products (4-hydroxybenzoic acid (P5), 3,4-
445 dihydroxybenzoic acid (P6), 2,3,4-trihydroxybenzoic acid (P7), and
446 2,3,4,5,6-pentahydroxybenzoic acid (P8)). There was found to be one
447 transition route for the continued ozonolysis of the hydroxylation products
448 that were produced in P6. The C2–C3 site of P6 to create P6-5O₃ ($\Delta G^\ddagger =$
449 16.59 kcal mol⁻¹) has the lowest activation energy of all the available paths
450 for the relevant reactions (**Fig. S11(b)**). This corresponds to a value of
451 16.59 kcal mol⁻¹. When the ΔG^\ddagger values of the breakage of five-membered
452 rings created by ozonolysis pathways are compared, one can get the
453 conclusion that the formation of IM_{P6}-5O₃-a is the most favored pathway.
454 All of the hydrogen abstraction processes involving H₂O and IM_{P6}-5O₃-a
455 have rather high energy barriers (32.93 kcal mol⁻¹). **On the other hand, in**
456 **Fig. S10(a), the very low ΔG^\ddagger values (19.74 ~ 22.89 kcal mol⁻¹) of the -**
457 **NO-O abstraction make it a desirable choice.** Following a chain of
458 ozonolysis reactions, the following products were obtained (**Fig.S11(c)**) :
459 ((2E,4Z)-2-formyl-4,5-dihydroxy-6-oxohexa-2,4-dienoic acid (P9); 2,3-
460 dihydroxymalealdehyde (P10); and 2,3-dioxpropanoic acid (P11).
461 Therefore, the product that was created, P10, may also be the product that

462 was discovered through experimentation (mass to charge ratios (m/z) = 115)
463 (Rana and Guzman, 2020). The VL subsequent reaction mechanism is
464 demonstrated in **Fig. S11(d)**. The final oxidation products of VL are P12
465 ((2E,4E)-4-formyl-2-methoxy-6-oxohexa-2,4-dienoic acid), P13 (ethene-
466 1,1,2-tricarbaldehyde), P14 (2-methoxy-2-oxoacetic acid), P15
467 (oxalaldehyde) and P16 ((E)-2-methoxy-4,5-dioxopent-2-enoic acid). The
468 formation of these products could explain the biomass burning material for
469 the formation of SOA (Rana and Guzman, 2022c).

470 **3.4 Comparison with available experimental results**

471 The rate constants (k) of the overall reaction under the temperature
472 range of 278–318 K were computed based on acquired potential energy
473 surfaces for the O_3 -initiated and HO^\bullet -initiated reactions of selected
474 compounds. The results of these calculations are listed in **Table S5** and **S6**,
475 respectively. The temperature dependences of the various k values for Ph,
476 4-HBA, and VL at the A-W interface and in bulk water are depicted in **Fig.**
477 **7**. At low values of k , there is a positive dependence on temperature. When
478 the k values are raised to a certain degree, the temperature dependency
479 seems to lose any significance it may have had before. The following is an
480 order of the k values for O_3 -initiated reactions: $A-W_{Ph} > TiO_2_{VL} > A-W_{VL} >$
481 $A-W_{4-HBA} > TiO_2_{4-HBA} > TiO_2_{Ph}$ (**Fig. 7(a)**). According to **Fig. 7(b)**, the k
482 values of HO^\bullet -initiated reactions go as follows: $TiO_2_{VL} > A-W_{Ph} > A-W_{VL} >$
483 $TiO_2_{4-HBA} > TiO_2_{Ph} > A-W_{4-HBA}$. In **Fig. 7(a)** and **Fig. 7(b)**, the k values of

484 HO[•]-initiated reactions are one hundred times greater than those of O₃-
485 initiated reactions. **Table 1** is a listing of the experimental and estimated *k*
486 values that are available for O₃-initiated and HO[•]-initiated reactions at 298
487 K. According to the findings, the ozonolysis of Ph was promoted by the
488 water-gas interface as well as by TiO₂ clusters, and the HO[•] initiated
489 reactions of VL were promoted by TiO₂ clusters. However, the O₃/HO[•] +
490 4-HBA reactions have the lowest *k* values among the three molecules when
491 tested in a variety of environmental environments. The estimated *k*_{O₃+Ph}
492 values at the A-W interface are 11 orders of magnitude greater than those
493 of catechol under dry conditions in gas phase (Zein et al., 2015), when
494 compared with the experimental data. Because it has a higher *k*_{O₃} value,
495 catechol, which is one of the main products of Ph's oxidation in the
496 atmosphere, has a higher degree of reactivity than its parent compound
497 (**Table 1**). The estimated value of VL is lower than the experimentally
498 determined value of *k*_{O₃} for guaiacol under dry conditions, which is (0.40
499 ± 0.31) × 10⁻¹⁸ cm³ molecule⁻¹ s⁻¹ in the gas phase (Zein et al., 2015).
500 The difference between the predicted value of *k*_{HO[•]+VL} is 1.14 × 10⁻¹⁰ cm³
501 molecule⁻¹ s⁻¹ and the average experimental value of *k*_{HO[•]} for
502 methoxyphenols is just an order of magnitude. As a consequence, the
503 findings of our calculations are reliable. **Previous studies measured the**
504 **second order rate constants of guaiacylacetone + HO[•] reaction to be (14–25)**
505 **× 10⁹ M⁻¹ s⁻¹ at pH 5 and 6 at aqueous secondary organic aerosol, which is**

506 lower than our results (Arciva et al., 2022). This is because galactose
507 reduces the steady-state concentration of HO[•]. The reaction rate constants
508 of PhCs increase with increasing pH and we calculated the rate constants
509 at pH 7 in bulk water (Ma et al., 2021). This study summarizes the O₃- and
510 HO[•]-initiated reaction sequences of three PhCs in different environmental
511 media. The reaction sequences for O₃- and HO[•]-initiated reactions of Ph
512 and 4-HBA are identical in different environmental media, while VL shows
513 slight variations. For O₃-initiated reactions, the reaction sequences are as
514 follows: Ph: A-W interface > Bulk water > Gas phase > TiO₂ clusters; 4-
515 HBA: Bulk water > A-W interface > TiO₂ clusters > Gas phase; VL: Bulk
516 water > TiO₂ clusters > A-W interface > Gas phase. For HO[•]-initiated
517 reactions, the sequences are: Ph: A-W interface ≈ Bulk water > Gas phase >
518 TiO₂ clusters; 4-HBA: Bulk water > A-W interface > TiO₂ clusters > Gas
519 phase; VL: TiO₂ clusters > Bulk water > A-W interface > Gas phase.
520 According to the atmospheric concentration of O₃, the atmospheric lifetime
521 of Ph is the shortest (< 1s) of the three PhCs at the gas-water interface or
522 bulk water, whereas 4-HBA and VL were oxidized more slowly than Ph
523 (Smith et al., 2016). See **Text S9** for ecotoxicity assessment.

524 **4. Conclusions**

525 Combining molecular dynamic simulations (with the AMBER force
526 field) and quantum chemical calculations (at the M06-2X/6-
527 311++G(3df,2p)//M06-2X/6-31+G(d,p) level) methods has provided

528 comprehensive insights into the surface properties of Ph, 4-HBA, and VL,
529 as well as their reactions induced by O₃ and HO[•], both in homogeneous and
530 heterogeneous environments. Here are some key findings from this
531 research:

532 (1) Free energy well of Ph, 4-HBA, and VL favor the A-W interface as
533 their preferred location, with the occurrence percentages of approximately
534 ~72%, ~68%, and ~73% respectively. Ph and 4-HBA show a preference for
535 the A-W interface over the air, with energy difference of around 0.22 and
536 0.45 kcal mol⁻¹. The VL adsorbed on the TiO₂ clusters has a higher
537 likelihood of remaining compared to VL adsorbed at the A-W interface. (2)
538 The adsorption capacity of TiO₂ clusters decreases with increasing cluster
539 size until $n > 4$. After that point, the adsorption capacity remains constant.
540 Strong electrostatic attractive interactions and attractive dispersion effects
541 occur between the benzene of the Ph and Ti atoms. Hydrogen bonds form
542 between the atom of O_{TiO₂} and the H-CHO group of 4-HBA or VL. (3) The
543 O₃- and HO[•]-initiated reactions for Ph and VL are facilitated by the A-W
544 interface and TiO₂ clusters, respectively, For O₃-initiated reactions at the
545 A-W interface, the C1–C2 position on the benzene ring is most favorable.
546 In both the A-W interface and on TiO₂ clusters, the total branching ratio for
547 routes R_{RAF} and R_{HAASub} is 72.68% ~ 100%. For route R_{HAASub}, the order
548 is H-CHO atom > H-OCH₃ atom > H-OH atom. (4) The k values (in
549 molecules·cm⁻³ s⁻¹, at 298K and 1 atm) of O₃-initiated reactions follow

550 the order of $A-W_{Ph}$ (5.98×10^{-7}) $>$ TiO_2_{VL} (3.30×10^{-15}) $>$ $A-W_{VL}$ (1.27
551 $\times 10^{-17}$) $>$ $A-W_{4-HBA}$ (6.79×10^{-23}) $>$ TiO_2_{4-HBA} (5.32×10^{-24}) $>$ TiO_2_{Ph}
552 (1.84×10^{-24}). The k values of HO^\bullet -initiated reactions follow the order of
553 TiO_2_{VL} (6.70×10^{-6}) $>$ $A-W_{Ph}$ (2.69×10^{-6}) $>$ $A-W_{VL}$ (1.73×10^{-7}) $>$ TiO_2
554 $_{4-HBA}$ (3.16×10^{-9}) $>$ TiO_2_{Ph} (3.17×10^{-10}) $>$ $A-W_{4-HBA}$ (9.49×10^{-11}). (5)
555 Toxicity risk assessment on aquatic species reveal that most of the reaction
556 products are significantly less harmful than the parent compounds.
557 However, products P1, P2, P3, P10, and P11 are more hazardous, and
558 further investigation of their atmospheric fate is recommended.

559 Ph undergoes transformation to malealdehyde and catechol when
560 exposed to O_3 or HO^\bullet in the troposphere (Xu and Wang, 2013). When
561 Ph/VL is at the droplet aerosol interface, rapid oxidation to
562 polyhydroxylated compounds occurs (Ma et al., 2021). VL eventually
563 creates tiny molecule aldehydes and acids. This is consistent with
564 experimental observations (Rana and Guzman, 2020). This oxidation
565 process is accelerated when VL is encased in a mineral aerosol represented
566 by TiO_2 clusters. Li et al. found that seasonal average concentrations of
567 total nitrophenol compounds in particulate matter were comparable to
568 those measured in the gas phase (Li et al., 2022). However, the reactivity
569 order of nitrophenols in the atmospheric compartments is water droplets $>$
570 gas phase $>$ particles (Vione et al., 2009). The formation of some low
571 molecular weight acids and aldehydes (2,3-dihydroxymalealdehyde, 2,3-

572 dioxpropanoic acid, etc.) confirms their association with the formation of
573 SOA. It is recommended that enterprises producing lignin, such as those in
574 the pulp and paper industry, or factories that employ lignin in the
575 manufacturing of adhesives, rust inhibitors, color dispersants, diluents, or
576 other similar products, be constructed in regions with low relative humidity.
577 It is recommended that treatment facilities that collect lignin pyrolysis
578 products and recycle the byproducts be located in the surrounding area.

579 **Data availability**

580 Data related to this article are available online at
581 <https://doi.org/10.5281/zenodo.10614650>.

582 **Author contributions**

583 Yanru Huo contributed to the manuscript conceptualization, methodology,
584 software, formal analysis, investigation, and writing of the original
585 manuscript. Mingxue Li provided insight into the writing ideas throughout
586 the article. Xueyu Wang offered some guidance on the method section of
587 the manuscript. Jianfei Sun, Yuxin Zhou, and Ma Yuhui reviewed the
588 original manuscript. Maoxia He: Conceptualization, Resources, Writing –
589 review & editing, Supervision, Funding acquisition.

590 **Competing interests**

591 The contact author has declared that none of the authors has any competing
592 interests.

593 **Acknowledgements**

594 This work was financially supported by the National Natural Science
595 Foundation of China (NSFC No. 22276109, 21777087, and 21876099).

596 Reference

597 Aracri, E., Tzanov, T., and Vidal, T.: Use of Cyclic Voltammetry as an
598 Effective Tool for Selecting Efficient Enhancers for Oxidative
599 Bioprocesses: Importance of pH, *Ind Eng Chem Res*, 52, 1455-1463,
600 <https://doi.org/10.1021/ie3027586>, 2013.

601 Arciva, S., Niedek, C., Mavis, C., Yoon, M., Sanchez, M. E., Zhang, Q.,
602 and Anastasio, C.: Aqueous $\cdot\text{OH}$ Oxidation of Highly Substituted
603 Phenols as a Source of Secondary Organic Aerosol, *Environ. Sci.*
604 *Technol.*, 56, 9959-9967, <https://doi.org/10.1021/acs.est.2c02225>,
605 2022.

606 Atkinson, R.: Kinetics and mechanisms of the gas-phase reactions of the
607 hydroxyl radical with organic compounds under atmospheric
608 conditions, *Chem. Rev*, 86, 69-201,
609 <https://doi.org/10.1021/cr00071a004>, 1986.

610 Bai, F.-Y., Ni, S., Ren, Y., Tang, Y.-Z., Zhao, Z., and Pan, X.-M.: DFT
611 analysis on the removal of dimethylbenzoquinones in atmosphere and
612 water environments: $\cdot\text{OH}$ -initiated oxidation and captured by $(\text{TiO}_2)_n$
613 clusters ($n=1-6$), *J Haz Mat*, 386, 121636,
614 <https://doi.org/10.1016/j.jhazmat.2019.121636>, 2020.

615 Banerjee, S., Gnanamani, E., Yan, X., and Zare, R. N.: Can all bulk-phase

-
- 616 reactions be accelerated in microdroplets?, *Analyst*, 142, 1399-1402,
617 <https://doi.org/10.1039/C6AN02225A>, 2017.
- 618 Bond, T. C., Streets, D. G., Yarber, K. F., Nelson, S. M., Woo, J.-H., and
619 Klimont, Z.: A technology-based global inventory of black and organic
620 carbon emissions from combustion, *J Geophys Res-Atmos*, 109,
621 <https://doi.org/10.1029/2003JD003697>, 2004.
- 622 Cao, H., Wang, K., Yang, Z., Wu, S., and Han, D.: Quantum chemical study
623 on the ozonolysis mechanism of guaiacol and the structure-reactivity
624 relationship of phenols with hydroxyl, methoxy, and methyl
625 substituents, *Chem. Eng.J.*, 420, 127629,
626 <https://doi.org/10.1016/j.cej.2020.127629>, 2021.
- 627 Carena, L., Zoppi, B., Sordello, F., Fabbri, D., Minella, M., and Minero, C.:
628 Phototransformation of Vanillin in Artificial Snow by Direct Photolysis
629 and Mediated by Nitrite, *Environ. Sci. Technol.*,
630 <https://doi.org/10.1021/acs.est.3c01931>, 2023.
- 631 Chen, C., Chen, H., Yu, J., Han, C., Yan, G., and Guo, S.: p-Nitrophenol
632 Removal by Bauxite Ore Assisted Ozonation and its Catalytic Potential,
633 *CLEAN – Soil, Air, Water*, 43, 1010-1017,
634 <https://doi.org/10.1002/clen.201400330>, 2015.
- 635 Chen, J., Li, C., Ristovski, Z., Milic, A., Gu, Y., Islam, M. S., Wang, S.,
636 Hao, J., Zhang, H., and He, C.: A review of biomass burning: Emissions
637 and impacts on air quality, health and climate in China, *Sci Total*

-
- 638 Environ, <https://doi.org/10.1016/j.scitotenv.2016.11.025>, 2017.
- 639 Chen, P., Li, Y., Zhang, Y., Xue, C., Hopke, P. K., and Li, X.: Dynamic
640 Changes of Composition of Particulate Matter Emissions during
641 Residential Biomass Combustion, *Environ. Sci. Technol.*, *57*, 15193-
642 15202, <https://doi.org/10.1021/acs.est.3c05412>, 2023.
- 643 Diehl, B. G., Brown, N. R., Frantz, C. W., Lumadue, M. R., and Cannon,
644 F.: Effects of pyrolysis temperature on the chemical composition of
645 refined softwood and hardwood lignins, *Carbon*, *60*, 531-537,
646 <https://doi.org/10.1016/j.carbon.2013.04.087>, 2013.
- 647 Finewax, Z., de Gouw, J. A., and Ziemann, P. J.: Identification and
648 Quantification of 4-Nitrocatechol Formed from OH and NO₃ Radical-
649 Initiated Reactions of Catechol in Air in the Presence of NO_x:
650 Implications for Secondary Organic Aerosol Formation from Biomass
651 Burning, *Environ. Sci. Technol.*, *52*, 1981-1989,
652 <https://doi.org/10.1021/acs.est.7b05864>, 2018.
- 653 Frisch, M. J., Trucks, G. W., Schlegel, H. B., Scuseria, G. E., Robb, M. A.,
654 Cheeseman, J. R., Scalmani, G., Barone, V., Petersson, G. A., Nakatsuji,
655 H., Li, X., Caricato, M., Marenich, A. V., Bloino, J., Janesko, B. G.,
656 Gomperts, R., Mennucci, B., Hratchian, H. P., Ortiz, J. V., Izmaylov, A.
657 F., Sonnenberg, J. L., Williams, Ding, F., Lipparini, F., Egidi, F., Goings,
658 J., Peng, B., Petrone, A., Henderson, T., Ranasinghe, D., Zakrzewski,
659 V. G., Gao, J., Rega, N., Zheng, G., Liang, W., Hada, M., Ehara, M.,

660 Toyota, K., Fukuda, R., Hasegawa, J., Ishida, M., Nakajima, T., Honda,
661 Y., Kitao, O., Nakai, H., Vreven, T., Throssell, K., Montgomery Jr., J.
662 A., Peralta, J. E., Ogliaro, F., Bearpark, M. J., Heyd, J. J., Brothers, E.
663 N., Kudin, K. N., Staroverov, V. N., Keith, T. A., Kobayashi, R.,
664 Normand, J., Raghavachari, K., Rendell, A. P., Burant, J. C., Iyengar,
665 S. S., Tomasi, J., Cossi, M., Millam, J. M., Klene, M., Adamo, C.,
666 Cammi, R., Ochterski, J. W., Martin, R. L., Morokuma, K., Farkas, O.,
667 Foresman, J. B., and Fox, D. J.: Gaussian 16 Rev. C.01 [code], 2016.

668 Gao, Y., Li, G., Qin, Y., Ji, Y., Mai, B., and An, T.: New theoretical insight
669 into indirect photochemical transformation of fragrance nitro-musks:
670 Mechanisms, eco-toxicity and health effects, *Environ Int*, 129, 68-75,
671 <https://doi.org/10.1016/j.envint.2019.05.020>, 2019.

672 Grassian, V. H.: New Directions: Nanodust – A source of metals in the
673 atmospheric environment? *Atmos Environ*, 43, 4666-4667,
674 <https://doi.org/10.1016/j.atmosenv.2009.06.032>, 2009.

675 Guzman, M. I., Pillar-Little, E. A., and Eugene, A. J.: Interfacial Oxidative
676 Oligomerization of Catechol, *ACS Omega*, 7, 36009-36016,
677 <https://doi.org/10.1021/acsomega.2c05290>, 2022.

678 Hawthorne, S. B., Krieger, M. S., Miller, D. J., and Mathiason, M. B.:
679 Collection and quantitation of methoxylated phenol tracers for
680 atmospheric pollution from residential wood stoves, *Environ. Sci.*
681 *Technol.*, 23, 470-475, <https://doi.org/10.1021/es00181a013>, 1989.

-
- 682 Henry, F., Coeur-Tourneur, C., Ledoux, F., Tomas, A., and Menu, D.:
683 Secondary organic aerosol formation from the gas phase reaction of
684 hydroxyl radicals with m-, o- and p-cresol, *Atmos Environ*, 42, 3035-
685 3045, <https://doi.org/10.1016/j.atmosenv.2007.12.043>, 2008.
- 686 Hub, J. S., de Groot, B. L., and van der Spoel, D.: g_wham—A Free
687 Weighted Histogram Analysis Implementation Including Robust Error
688 and Autocorrelation Estimates, *J. Chem. Theory Comput.*, 6, 3713-
689 3720, <https://doi.org/10.1021/ct100494z>, 2010.
- 690 Humphrey, W., Dalke, A., and Schulten, K.: VMD: Visual molecular
691 dynamics, *J Mol Graph Model*, 14, 33-38,
692 [https://doi.org/10.1016/0263-7855\(96\)00018-5](https://doi.org/10.1016/0263-7855(96)00018-5), 1996.
- 693 Ito, A. and Penner, J. E.: Historical emissions of carbonaceous aerosols
694 from biomass and fossil fuel burning for the period 1870–2000, *Global*
695 *Biogeochem Cy*, 19, <https://doi.org/10.1029/2004GB002374>, 2005.
- 696 Jämbeck, J. P. and Lyubartsev, A. P.: Update to the general amber force
697 field for small solutes with an emphasis on free energies of hydration,
698 *J Phys Chem B*, 118, 3793-3804, <https://doi.org/10.1021/jp4111234>,
699 2014.
- 700 Jiang, W., Niedek, C., Anastasio, C., and Zhang, Q.: Photoaging of
701 phenolic secondary organic aerosol in the aqueous phase: evolution of
702 chemical and optical properties and effects of oxidants, *Atmos. Chem.*
703 *Phys.*, 23, 7103-7120, <https://doi.org/10.5194/acp-23-7103-2023>, 2023.

-
- 704 Kroflič, A., Huš, M., Grilc, M., and Grgić, I.: Underappreciated and
705 Complex Role of Nitrous Acid in Aromatic Nitration under Mild
706 Environmental Conditions: The Case of Activated Methoxyphenols,
707 Environ. Sci. Technol., 52, 13756-13765,
708 <https://doi.org/10.1021/acs.est.8b01903>, 2018.
- 709 Kumar, S., Rosenberg, J. M., Bouzida, D., Swendsen, R. H., and Kollman,
710 P. A.: THE weighted histogram analysis method for free-energy
711 calculations on biomolecules. I. The method, J Comput Chem, 13,
712 1011-1021, <https://doi.org/10.1002/jcc.540130812>, 1992.
- 713 Kusaka, R., Nihonyanagi, S., and Tahara, T.: The photochemical reaction
714 of phenol becomes ultrafast at the air–water interface, Nat Chem, 13,
715 306-311, <https://doi.org/10.1038/s41557-020-00619-5>, 2021.
- 716 Lee, J. K., Banerjee, S., Nam, H. G., and Zare, R. N.: Acceleration of
717 reaction in charged microdroplets, Q. Rev. Biophys., 48, 437-444,
718 <https://doi.org/10.1017/S0033583515000086>, 2015a.
- 719 Lee, J. K., Kim, S., Nam, H. G., and Zare, R. N.: Microdroplet fusion mass
720 spectrometry for fast reaction kinetics, PANS, 112, 3898-3903,
721 <https://doi.org/10.1073/pnas.1503689112>, 2015b.
- 722 Lelieveld, J., Gromov, S., Pozzer, A., and Taraborrelli, D.: Global
723 tropospheric hydroxyl distribution, budget and reactivity, Atmos.
724 Chem. Phys., 16, 12477-12493, [https://doi.org/10.5194/acp-16-12477-](https://doi.org/10.5194/acp-16-12477-2016)
725 [2016](https://doi.org/10.5194/acp-16-12477-2016), 2016.

-
- 726 Li, M., Wang, X., Zhao, Y., Du, P., Li, H., Li, J., Shen, H., Liu, Z., Jiang,
727 Y., Chen, J., Bi, Y., Zhao, Y., Xue, L., Wang, Y., Chen, J., and Wang,
728 W.: Atmospheric Nitrated Phenolic Compounds in Particle, Gaseous,
729 and Aqueous Phases During Cloud Events at a Mountain Site in North
730 China: Distribution Characteristics and Aqueous-Phase Formation, *J*
731 *Geophys Res-Atmos*, 127, <https://doi.org/10.1029/2022JD037130>,
732 2022.
- 733 Liao, Y., Koelewijn, S.-F., Van den Bossche, G., Van Aelst, J., Van den
734 Bosch, S., Renders, T., Navare, K., Nicolai, T., Van Aelst, K., Maesen,
735 M., Matsushima, H., Thevelein, J. M., Van Acker, K., Lagrain, B.,
736 Verboekend, D., and Sels, B. F.: A Sustainable Wood Biorefinery for
737 Low-Carbon Footprint Chemicals Production, *Science*, 367, 1385-
738 1390, <https://doi.org/10.1126/science.aau1567>, 2020.
- 739 Lin, P.-C., Wu, Z.-H., Chen, M.-S., Li, Y.-L., Chen, W.-R., Huang, T.-P.,
740 Lee, Y.-Y., and Wang, C. C.: Interfacial Solvation and Surface pH of
741 Phenol and Dihydroxybenzene Aqueous Nanoaerosols Unveiled by
742 Aerosol VUV Photoelectron Spectroscopy, *J Phys Chem B*, 121, 1054-
743 1067, <https://doi.org/10.1021/acs.jpcc.6b10201>, 2017.
- 744 Liu, C., Chen, D., and Chen, X. e.: Atmospheric Reactivity of
745 Methoxyphenols: A Review, *Environ. Sci. Technol.*, 56, 2897-2916,
746 <https://doi.org/10.1021/acs.est.1c06535>, 2022.
- 747 Liu, C., Liu, J., Liu, Y., Chen, T., and He, H. J. A. e.: Secondary organic

-
- 748 aerosol formation from the OH-initiated oxidation of guaiacol under
749 different experimental conditions, *Atmos Environ*, 207, 30-37,
750 <https://doi.org/10.1016/j.atmosenv.2019.03.021>, 2019.
- 751 Lou, R., Wu, S.-b., and Lv, G.-j.: Effect of conditions on fast pyrolysis of
752 bamboo lignin, *J Anal Appl Pyrol*, 89, 191-196,
753 <https://doi.org/10.1016/j.jaap.2010.08.007>, 2010.
- 754 Lu, T. and Chen, F.: Multiwfn: A multifunctional wavefunction analyzer, *J*
755 *Comput Chem*, 33, 580-592, <https://doi.org/10.1002/jcc.22885>, 2012.
- 756 Lu, T. and Chen, Q.: Interaction Region Indicator: A Simple Real Space
757 Function Clearly Revealing Both Chemical Bonds and Weak
758 Interactions**, *Chemistry–Methods*, 1, 231-239,
759 <https://doi.org/10.1002/cmt.202100007>, 2021.
- 760 Ma, L., Guzman, C., Niedek, C., Tran, T., Zhang, Q., and Anastasio, C.:
761 Kinetics and Mass Yields of Aqueous Secondary Organic Aerosol from
762 Highly Substituted Phenols Reacting with a Triplet Excited State,
763 *Environ. Sci. Technol.*, 55, 5772-5781,
764 <https://doi.org/10.1021/acs.est.1c00575>, 2021.
- 765 Nollet, H., Roels, M., Lutgen, P., Van der Meeren, P., and Verstraete, W.:
766 Removal of PCBs from wastewater using fly ash, *Chemosphere*, 53,
767 655-665, [https://doi.org/10.1016/S0045-6535\(03\)00517-4](https://doi.org/10.1016/S0045-6535(03)00517-4), 2003.
- 768 Pillar-Little, E. A. and Guzman, M. I.: Oxidation of Substituted Catechols
769 at the Air–Water Interface: Production of Carboxylic Acids, Quinones,

-
- 770 and Polyphenols, *Environ. Sci. Technol.*, 51, 4951-4959,
771 <https://doi.org/10.1021/acs.est.7b00232>, 2017.
- 772 Pillar-Little, E. A., Camm, R. C., and Guzman, M. I.: Catechol Oxidation
773 by Ozone and Hydroxyl Radicals at the Air–Water Interface, *Environ.*
774 *Sci. Technol.*, 48, 14352-14360, <https://doi.org/10.1021/es504094x>,
775 2014.
- 776 Qu, Z.-w. and Kroes, G.-J.: Theoretical Study of the Electronic Structure
777 and Stability of Titanium Dioxide Clusters (TiO₂)_n with n = 1–9, *J Phys*
778 *Chem B*, 110, 8998-9007, <https://doi.org/10.1021/jp056607p>, 2006.
- 779 Rana, M. S. and Guzman, M. I.: Oxidation of Phenolic Aldehydes by
780 Ozone and Hydroxyl Radicals at the Air–Water Interface, *J Phys Chem*
781 *A*, 124, 8822-8833, <https://doi.org/10.1021/acs.jpca.0c05944>, 2020.
- 782 Rana, M. S. and Guzman, M. I.: Oxidation of Phenolic Aldehydes by
783 Ozone and Hydroxyl Radicals at the Air–Solid Interface, *Acs Earth*
784 *Space Chem*, 6, 2900-2909,
785 <https://doi.org/10.1021/acsearthspacechem.2c00206>, 2022a.
- 786 Rana, M. S. and Guzman, M. I.: Oxidation of Catechols at the Air–Water
787 Interface by Nitrate Radicals, *Environ. Sci. Technol.*, 56, 15437-15448,
788 <https://doi.org/10.1021/acs.est.2c05640>, 2022b.
- 789 Rana, M. S. and Guzman, M. I.: Surface Oxidation of Phenolic Aldehydes:
790 Fragmentation, Functionalization, and Coupling Reactions, *J Phys*
791 *Chem A*, 126, 6502-6516, <https://doi.org/10.1021/acs.jpca.2c04963>,

-
- 792 2022c.
- 793 Reid, J. S., Eck, T. F., Christopher, S. A., Koppman, R., Dubovik, O.,
794 Eleuterio, D. P., Holben, B. N., Reid, E. A., and Zhang, J.: A review of
795 biomass burning emissions part III: Intensive optical properties of
796 biomass burning particles, *Atmos. Chem. Phys.*, 5, 827-849,
797 <https://doi.org/10.5194/acp-5-827-2005>, 2005.
- 798 Roeselová, M., Vieceli, J., Dang, L. X., Garrett, B. C., and Tobias, D. J.:
799 Hydroxyl Radical at the Air–Water Interface, *J. Am. Chem. Soc.*, 126,
800 16308-16309, <https://doi.org/10.1021/ja045552m>, 2004.
- 801 Rogge, W. F., Hildemann, L. M., Mazurek, M. A., and Cass, G. R.: Sources
802 of Fine Organic Aerosol. 9. Pine, Oak, and Synthetic Log Combustion
803 in Residential Fireplaces, *Environ. Sci. Technol.*, 32, 13-22,
804 <https://doi.org/10.1021/es960930b>, 1998.
- 805 Rubasinghege, G., Elzey, S., Baltrusaitis, J., Jayaweera, P. M., and
806 Grassian, V. H.: Reactions on Atmospheric Dust Particles: Surface
807 Photochemistry and Size-Dependent Nanoscale Redox Chemistry, *J.*
808 *Phys. Chem. Lett.*, 1, 1729-1737, <https://doi.org/10.1021/jz100371d>,
809 2010.
- 810 Rynjah, S., Baro, B., and Sarkar, B.: Oxepin Derivatives Formation from
811 Gas-Phase Catechol Ozonolysis, *J Phys Chem A*, 128, 251-260,
812 <https://doi.org/10.1021/acs.jpca.3c04582>, 2024.
- 813 Sakata, K., Takahashi, Y., Takano, S., Matsuki, A., Sakaguchi, A., and

-
- 814 Tanimoto, H.: First X-ray Spectroscopic Observations of Atmospheric
815 Titanium Species: Size Dependence and the Emission Source, *Environ.*
816 *Sci. Technol.*, 55, 10975-10986,
817 <https://doi.org/10.1021/acs.est.1c02000>, 2021.
- 818 Shang, H., Wang, X., Li, H., Li, M., Mao, C., Xing, P., Zhao, S., Chen, Z.,
819 Sun, J., Ai, Z., and Zhang, L.: Oxygen vacancies promote sulfur species
820 accumulation on TiO₂ mineral particles, *Appl. Catal. B Environ.*, 290,
821 120024, <https://doi.org/10.1016/j.apcatb.2021.120024>, 2021.
- 822 Shi, Q., Zhang, W., Ji, Y., Wang, J., Qin, D., Chen, J., Gao, Y., Li, G., and
823 An, T.: Enhanced uptake of glyoxal at the acidic nanoparticle interface:
824 implications for secondary organic aerosol formation, *Environ Sci-*
825 *Nano*, 7, 1126-1135, <https://doi.org/10.1039/D0EN00016G>, 2020.
- 826 Simoneit, B. R. T.: Biomass burning — a review of organic tracers for
827 smoke from incomplete combustion, *Appl Geochem*, 17, 129-162,
828 [https://doi.org/10.1016/S0883-2927\(01\)00061-0](https://doi.org/10.1016/S0883-2927(01)00061-0), 2002.
- 829 Smith, J. D., Kinney, H., and Anastasio, C.: Phenolic carbonyls undergo
830 rapid aqueous photodegradation to form low-volatility, light-absorbing
831 products, *Atmos Environ*, 126, 36-44,
832 <https://doi.org/10.1016/j.atmosenv.2015.11.035>, 2016.
- 833 Soongpravit, K., Sricharoenchaikul, V., and Atong, D.: Phenol-derived
834 products from fast pyrolysis of organosolv lignin, *Energy Rep*, 6, 151-
835 167, <https://doi.org/10.1016/j.egy.2020.08.040>, 2020.

-
- 836 Sun, J., Han, D., Shallcross, D. E., Cao, H., Wei, B., Mei, Q., Xie, J., Zhan,
837 J., and He, M.: Theoretical studies on the heterogeneous ozonolysis of
838 syringol on graphene: Mechanism, kinetics and ecotoxicity assessment,
839 Chem. Eng.J., 404, 126484, <https://doi.org/10.1016/j.cej.2020.126484>,
840 2021a.
- 841 Sun, N., Rodríguez, H., Rahman, M., and Rogers, R. D.: Where are ionic
842 liquid strategies most suited in the pursuit of chemicals and energy
843 from lignocellulosic biomass?, Chem. Commun., 47, 1405-1421,
844 <https://doi.org/10.1039/C0CC03990J>, 2011.
- 845 Sun, Y., Chen, X., Xu, F., and Wang, X.: Quantum chemical calculations
846 on the mechanism and kinetics of ozone-initiated removal of p-
847 coumaryl alcohol in the atmosphere, Chemosphere, 253, 126744,
848 <https://doi.org/10.1016/j.chemosphere.2020.126744>, 2020.
- 849 Sun, Y., Chen, X., Liu, L., Xu, F., and Zhang, X.: Mechanisms and kinetics
850 studies of the atmospheric oxidation of eugenol by hydroxyl radicals
851 and ozone molecules, Sci Total Environ, 770, 145203,
852 <https://doi.org/10.1016/j.scitotenv.2021.145203>, 2021b.
- 853 Tomas, A., Olariu, R. I., Barnes, I., and Becker, K. H. J. I. J. o. C. K.:
854 Kinetics of the reaction of O₃ with selected benzenediols, 35, 223-230,
855 <https://doi.org/10.1002/kin.10121>, 2003.
- 856 Vione, D., Maurino, V., Minero, C., Duncianu, M., Olariu, R.-I., Arsene,
857 C., Sarakha, M., and Mailhot, G.: Assessing the transformation kinetics

-
- 858 of 2- and 4-nitrophenol in the atmospheric aqueous phase. Implications
859 for the distribution of both nitroisomers in the atmosphere, *Atmos*
860 *Environ*, 43, 2321-2327,
861 <https://doi.org/10.1016/j.atmosenv.2009.01.025>, 2009.
- 862 Wang, R., Li, K., Li, J., Tsona, N. T., Wang, W., and Du, L.: Interaction of
863 Acrylic Acid and SO₂ on the Surface of Mineral Dust Aerosol, *Acs*
864 *Earth Space Chem*, 7, 548-558,
865 <https://doi.org/10.1021/acsearthspacechem.2c00323>, 2023.
- 866 Xu, C. and Wang, L.: Atmospheric Oxidation Mechanism of Phenol
867 Initiated by OH Radical, *J Phys Chem A*, 117, 2358-2364,
868 <https://doi.org/10.1021/jp308856b>, 2013.
- 869 Yan, X., Bain, R. M., and Cooks, R. G.: Organic Reactions in
870 Microdroplets: Reaction Acceleration Revealed by Mass Spectrometry,
871 *Angew. Chem. Int. Ed.*, 55, 12960-12972,
872 <https://doi.org/10.1002/anie.201602270>, 2016.
- 873 Yao, L., Yang, L., Chen, J., Wang, X., Xue, L., Li, W., Sui, X., Wen, L.,
874 Chi, J., Zhu, Y., Zhang, J., Xu, C., Zhu, T., and Wang, W.:
875 Characteristics of carbonaceous aerosols: Impact of biomass burning
876 and secondary formation in summertime in a rural area of the North
877 China Plain, *Sci Total Environ*, 557-558, 520-530,
878 <https://doi.org/10.1016/j.scitotenv.2016.03.111>, 2016.
- 879 Yee, L. D., Kautzman, K. E., Loza, C. L., Schilling, K. A., Coggon, M. M.,

-
- 880 Chhabra, P. S., Chan, M. N., Chan, A. W. H., Hersey, S. P., Crounse, J.
881 D., Wennberg, P. O., Flagan, R. C., and Seinfeld, J. H.: Secondary
882 organic aerosol formation from biomass burning intermediates: Phenol
883 and methoxyphenols, *Atmos. Chem. Phys.*, 13, 8019-8043,
884 <https://doi.org/10.5194/acp-13-8019-2013>, 2013.
- 885 Yuan, S., Wang, X., Jiang, Z., Zhang, H., and Yuan, S.: Contribution of air-
886 water interface in removing PFAS from drinking water: Adsorption,
887 stability, interaction and machine learning studies, *Water Research*, 236,
888 119947, <https://doi.org/10.1016/j.watres.2023.119947>, 2023.
- 889 Zein, A. E., Coeur, C., Obeid, E., Lauraguais, A., and Fagniez, T.: Reaction
890 Kinetics of Catechol (1,2-Benzenediol) and Guaiacol (2-
891 Methoxyphenol) with Ozone, *J Phys Chem A*, 119, 6759-6765,
892 <https://doi.org/10.1021/acs.jpca.5b00174>, 2015.
- 893 Zhang, W., Ji, Y., Li, G., Shi, Q., and An, T.: The heterogeneous reaction
894 of dimethylamine/ammonia with sulfuric acid to promote the growth
895 of atmospheric nanoparticles, *Environ Sci-Nano*, 6, 2767-2776,
896 <https://doi.org/10.1039/C9EN00619B>, 2019.
- 897 Zhang, W., Tong, S., Jia, C., Wang, L., Liu, B., Tang, G., Ji, D., Hu, B., Liu,
898 Z., Li, W., Wang, Z., Liu, Y., Wang, Y., and Ge, M.: Different HONO
899 Sources for Three Layers at the Urban Area of Beijing, *Environ. Sci.*
900 *Technol.*, 54, 12870-12880, <https://doi.org/10.1021/acs.est.0c02146>,
901 2020.

902 Zhong, J., Kumar, M., Anglada, J. M., Martins-Costa, M. T. C., Ruiz-Lopez,
903 M. F., Zeng, X. C., and Francisco, J. S.: Atmospheric Spectroscopy and
904 Photochemistry at Environmental Water Interfaces, *Annu Rev Phys*
905 *Chem*, 70, 45-69, [https://doi.org/10.1146/annurev-physchem-042018-](https://doi.org/10.1146/annurev-physchem-042018-052311)
906 [052311](https://doi.org/10.1146/annurev-physchem-042018-052311), 2019.

907

908

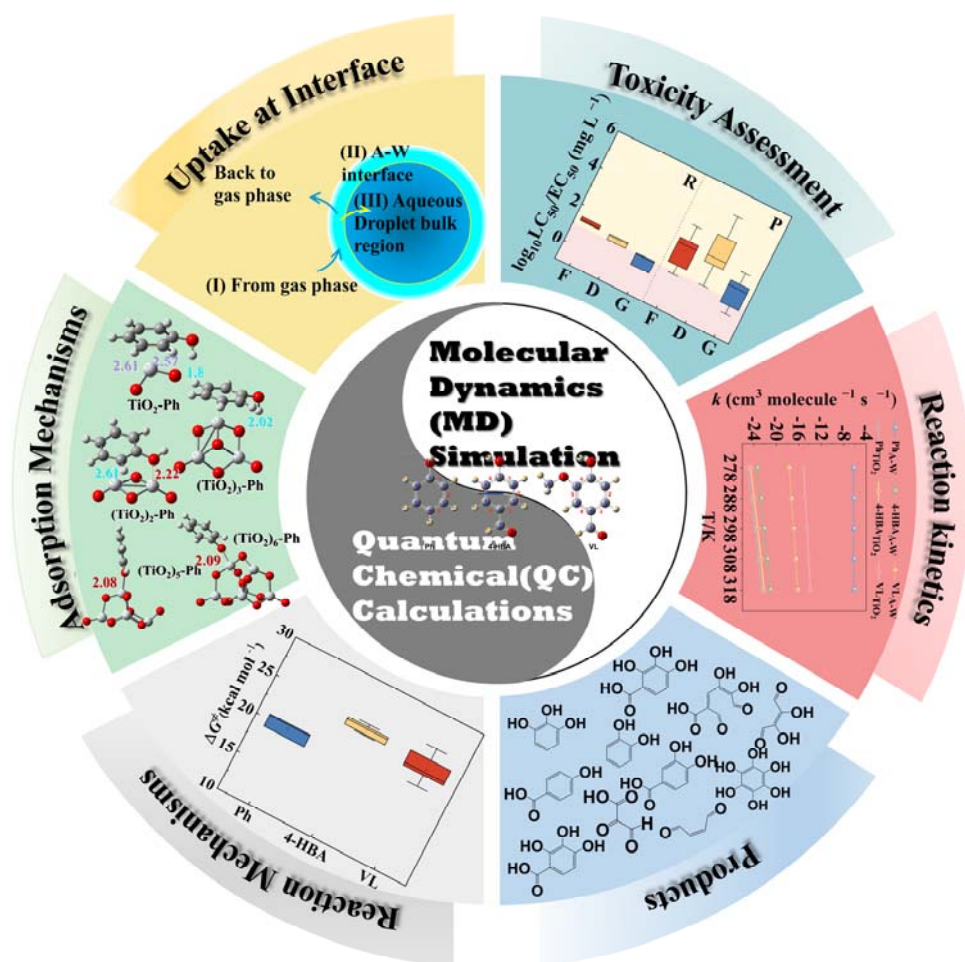
909

910

911

912

913



914

915

916

917

918

919

920

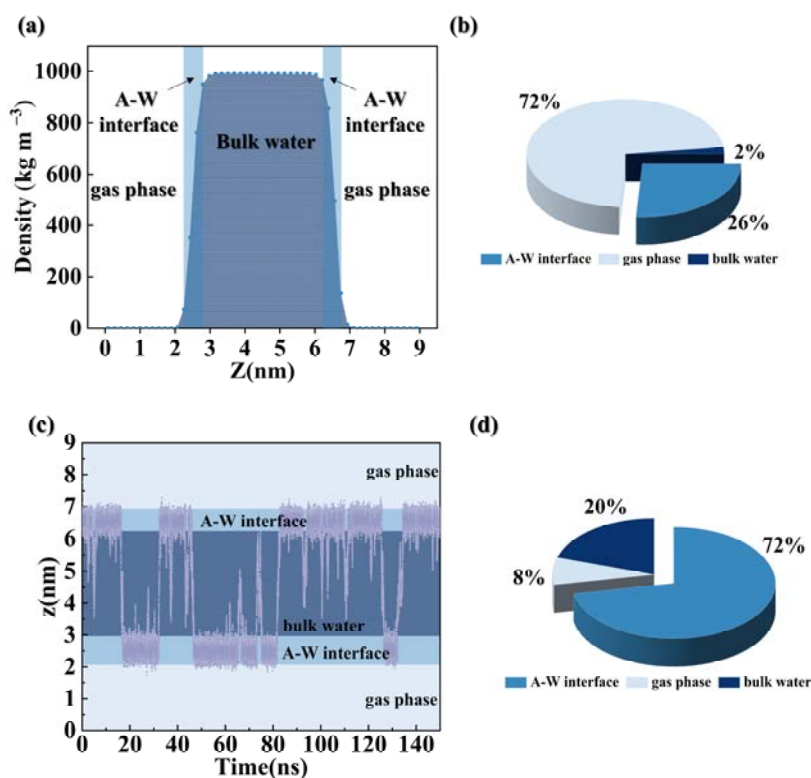
921

922

923

924

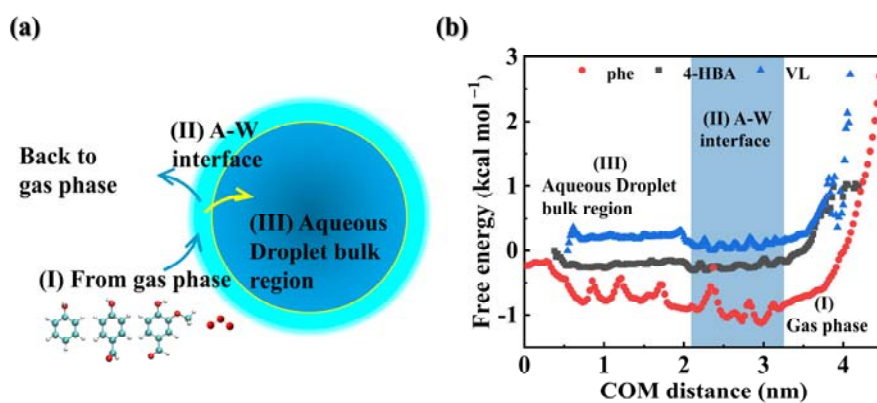
Graphical Abstract



925

926

927 **Fig.1 (a)** Relative concentration distributions in the A-W system along the z-axis; **(b)** probability of
 928 O_3 at the A-W interface, in gas phase, and in bulk water; **(c)** MD trajectories of Ph diffusion through
 929 the water slab over a 150 ns period; **(d)** probability of Ph at the A-W interface, in gas phase, and in
 930 bulk water.

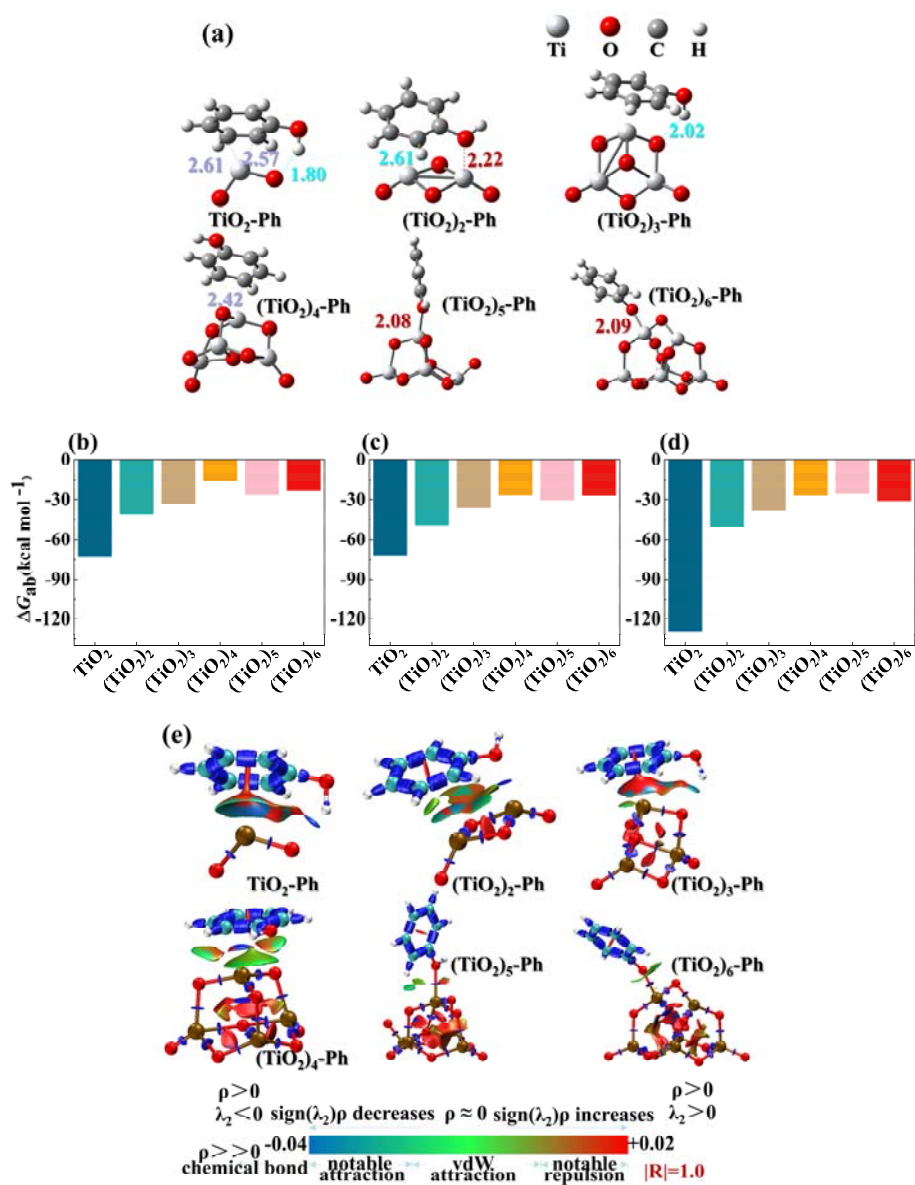


931

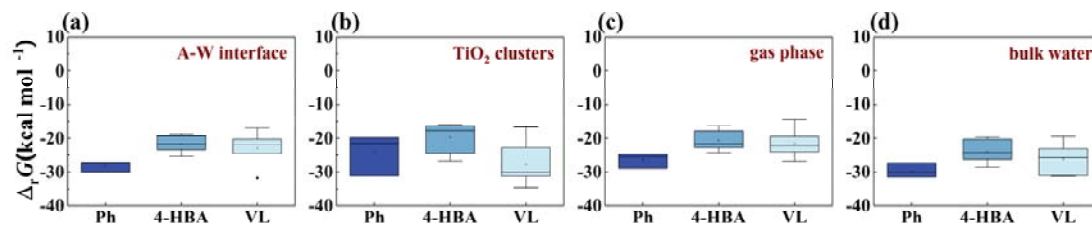
932 **Fig.2 (a)** Three key processes for the reaction of gaseous PhCs (Ph, 4-HBA, or VL) with the **water**
 933 **drops**; **(b)** free energy **change** profile of gaseous PhCs (Ph, 4-HBA, or VL) approaching the bulk

934 water.

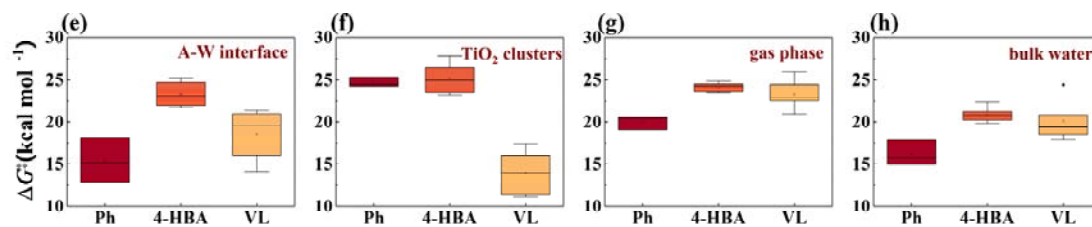
935



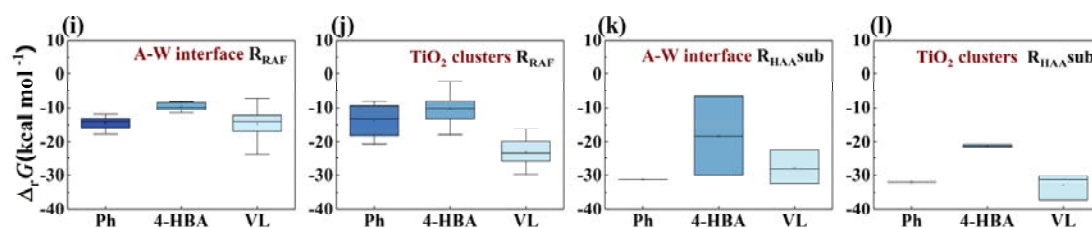
942



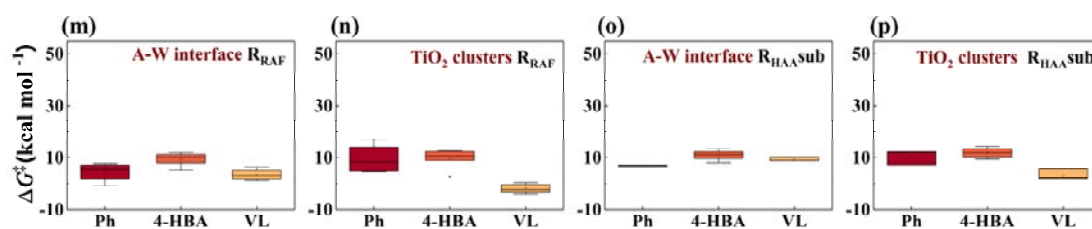
943

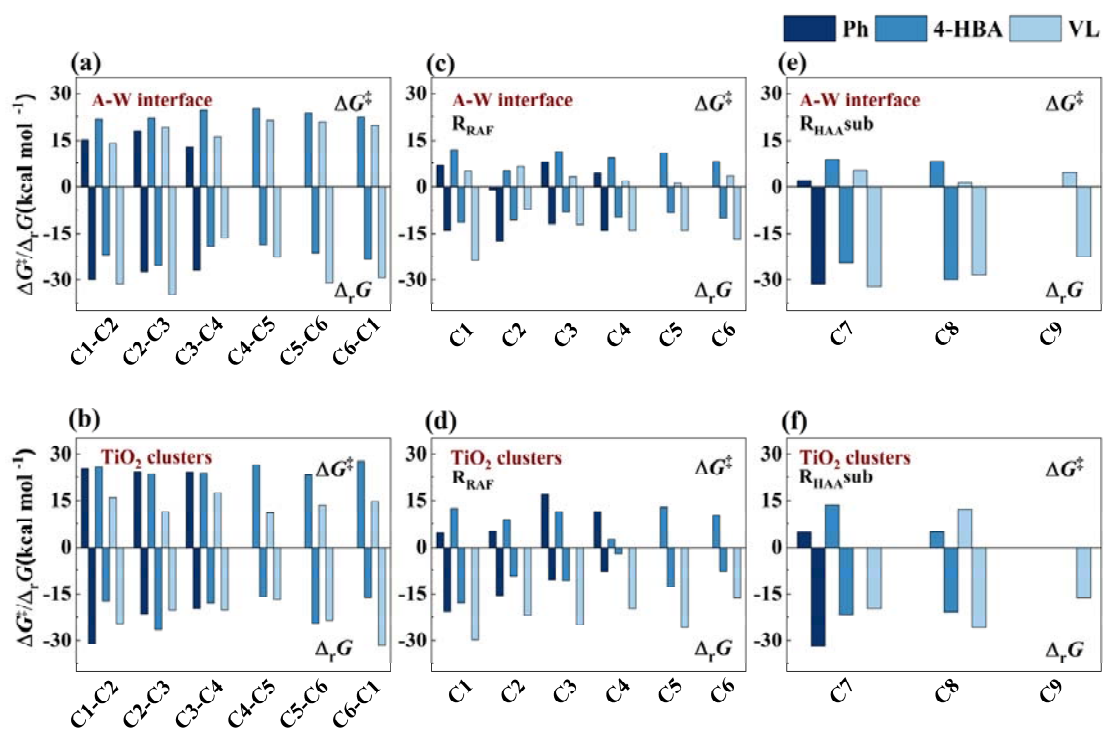


944



945

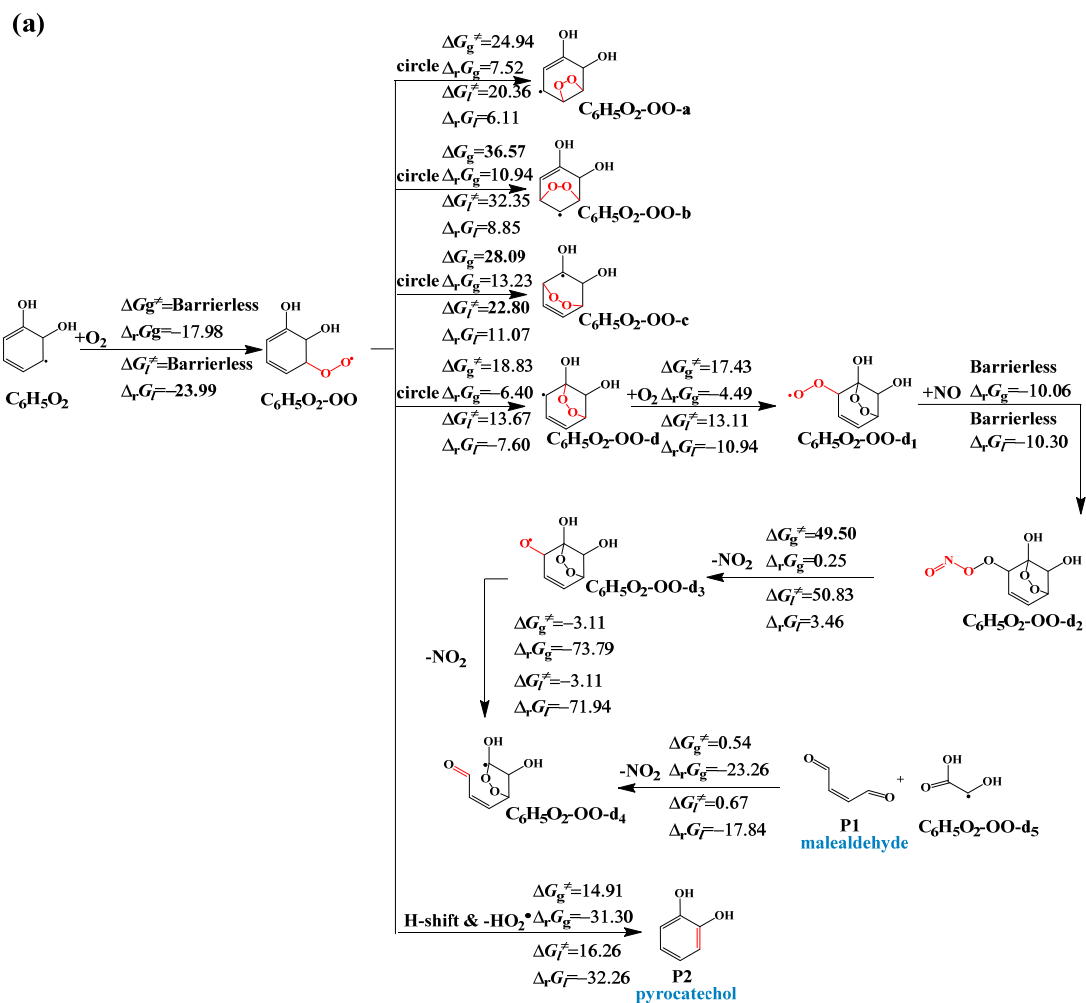
946 **Fig. 4** Statistical charts of calculated (a)–(d) $\Delta_r G$ and (e)–(h) ΔG^\ddagger values for O₃-initiated reactions;947 (i)–(l) $\Delta_r G$ and (m)–(p) ΔG^\ddagger values for HO[•]-initiated reactions.



948

949 **Fig.5** $\Delta_r G$ and ΔG^\ddagger values of (a)–(b) O₃-initiated reactions and (c)–(f) HO[•]-initiated reactions at

950 different reaction positions.

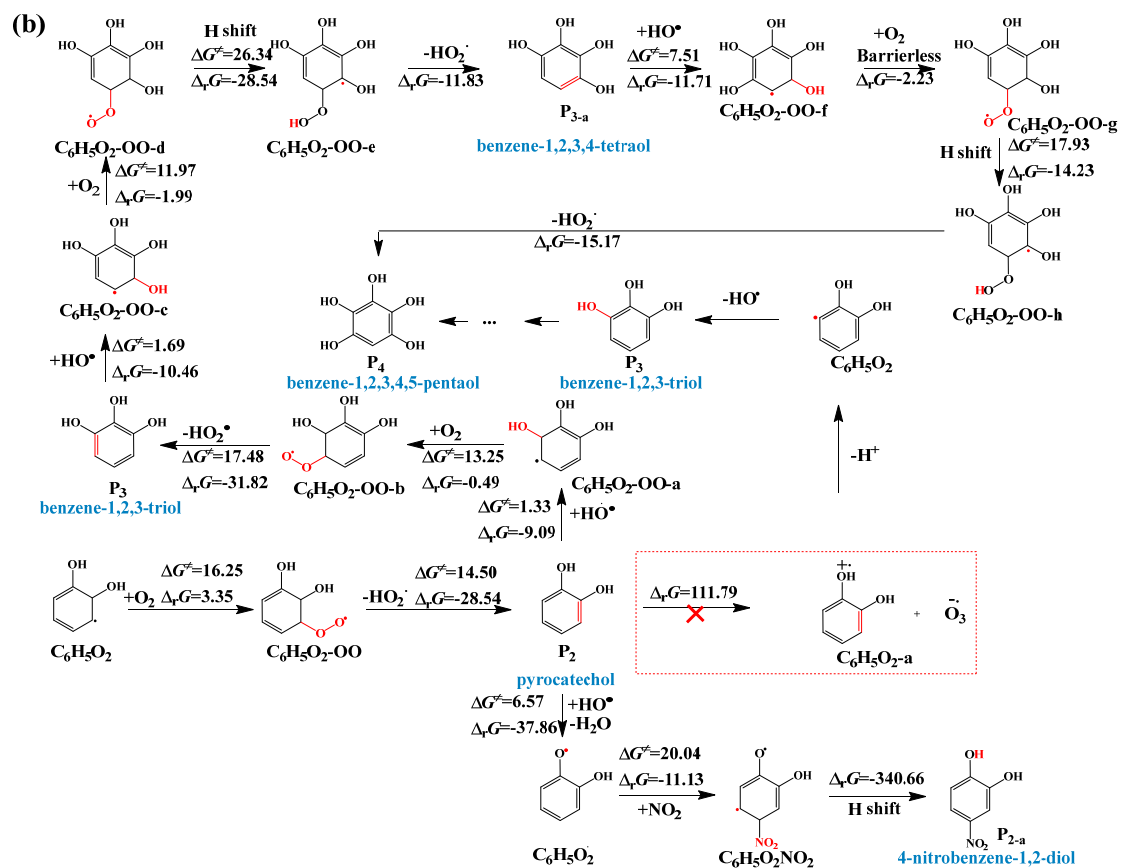


951

952 **Fig.6** Subsequent reaction mechanisms of important intermediates (IMs) (unit: kcal mol⁻¹) in (a)

953 gas phase (g) / bulk water (l) and at (b) A-W interface (Continue on the next page).

954



955

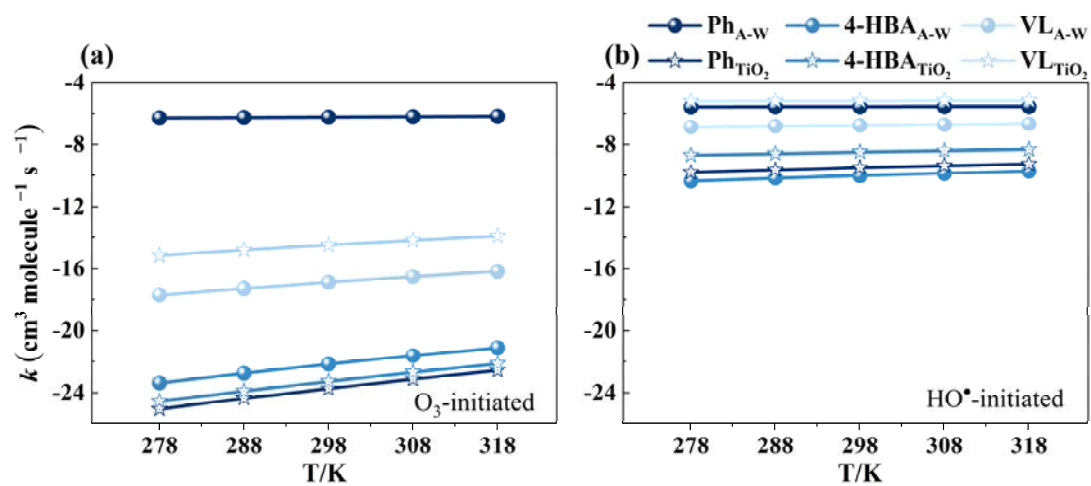
956 **Fig.6** (Continue) Subsequent reaction mechanisms of important intermediates (IMs) (unit: kcal mol957 ⁻¹) in (a) gas phase (g) / bulk water (l) and at (b) A-W interface.

958

959

960

961



962

963 **Fig. 7** Calculated rate constants for the initial reactions of Ph, 4-HBA, and VL with O_3 and HO^\bullet at

964 different temperatures (278–318 K) and 1 atm.

965

966

967

968

969

970

971

972

973

974

975

976

977

978

979 **Table 1** The available experimental and calculated reaction rate constants (k) values of O₃- and
 980 HO•-initiated reactions at 298 K. Unit: cm³ molecule⁻¹ s⁻¹.

Compounds	$k_{tot-A-W,cal}^a$	$k_{tot-TiO_2,cal}^b$	$k_{tot-gas,cal}^c$	$k_{tot-wat,cal}^d$	k_{exp}	Ref.
Ph	5.98×10^{-7}	1.84×10^{-24}	5.27×10^{-20}	4.02×10^{12}	$(13.5 \pm 1.1) \times 10^{-18,e}$	Zein et al. (2015)
	2.69×10^{-6}	3.17×10^{-10}	2.34×10^{-9}	4.46×10^{13}	—	
4-HBA	6.79×10^{-23}	5.32×10^{-24}	4.93×10^{-24}	1.97×10^{12}	—	
	9.49×10^{-11}	3.16×10^{-9}	7.90×10^{-11}	2.52×10^{13}	—	Rana et al. (2020)
VL	1.27×10^{-17}	3.30×10^{-15}	1.35×10^{-22}	2.20×10^{12}	$(0.40 \pm 0.31) \times 10^{-18,f}$	Zein et al. (2015)
	1.73×10^{-7}	6.70×10^{-6}	1.14×10^{-10}	3.15×10^{13}	$6.00 \times 10^{-11,g}$	Rana et al. (2020)

981 ^a: calculated values of phenolic compounds at A-W interface;

982 ^b: calculated values of phenolic compounds on TiO₂ clusters;

983 ^c: calculated values of phenolic compounds in the gas phase;

984 ^d: calculated values of phenolic compounds in the bulk water.

985 ^e: experimental values of catechol in the gas phase;

986 ^f: experimental values of guaiacol in the gas phase;

987 ^g: experimental average $k_{HO\bullet}$ values of methoxyphenols in the gas phase.